ELSEVIER

Earth and Planetary Science Letters 199 (2002) 227–241

EPSL

www.elsevier.com/locate/epsl

# The effect of $Al_2O_3$ on Fe–Mg partitioning between magnesiowüstite and magnesium silicate perovskite

Daniel J. Frost *, Falko Langenhorst

*Bayerisches Geoinstitut, Universität Bayreuth, D-95440, Bayreuth, Germany*

Received 17 October 2001; received in revised form 4 January 2002; accepted 20 February 2002

**Abstract**

We have measured the partitioning of $Fe^{2+}$, $Fe^{3+}$ and $Mg^{2+}$ between magnesiowüstite and magnesium silicate perovskite in both $Al_2O_3$-bearing and $Al_2O_3$-free systems. Starting compositions with varying Fe/(Fe+Mg) molar ratios were equilibrated in a multianvil apparatus between 24 and 25 GPa and 1650–1900°C. A time study indicated that run durations of at least 8 h were required for the partitioning to reach equilibrium at 1650°C. Multi-chamber rhenium metal capsules were employed that provided relatively oxidising conditions and allowed up to eight starting materials to be equilibrated in a single experiment. In the $Al_2O_3$-free system Fe partitions preferentially into magnesiowüstite. In the $Al_2O_3$-bearing system, however, the proportion of Fe that partitions into perovskite increases with the perovskite $Al_2O_3$ content. The Fe–Mg distribution between the phases has been parameterised as a function of the perovskite $Al_2O_3$ concentration and we observe the $Al_2O_3$ dependence to be non-linear. The $Fe^{3+}/\Sigma Fe$ ratios of coexisting perovskite and magnesiowüstite crystals were measured using electron energy-loss near-edge structure (ELNES) spectroscopy. In the $Al_2O_3$-bearing system perovskite $Fe^{3+}/\Sigma Fe$ ratios range between 60 and 80%, which is over three times greater than that measured for $Al_2O_3$-free perovskite. The results imply that increasing the $Al_2O_3$ content of perovskite only increases the $Fe^{3+}$ solubility and has no measurable effect on the $Fe^{2+}$ partitioning between magnesiowüstite and perovskite. The variation in the $Fe^{3+}$ solubility with the $Al^{3+}$ content of perovskite is non-linear. We propose that this results from substitution of $Fe^{3+}$ onto the perovskite six-fold coordinated site for low $Al^{3+}$ concentrations but substitution of a $FeAlO_3$ component at higher $Al^{3+}$ contents, where $Fe^{3+}$ is on the eight-fold site charge balanced by Al on the six-fold coordinated site. A comparison with our experimental data suggests that the Fe partitioning between some $(Mg,Fe)SiO_3$ and (Mg,Fe)O inclusions found in diamonds is quite consistent with their origin as perovskite and magnesiowüstite in the lower mantle. The partitioning between some (Mg,Fe)O and $(Mg,Fe,Al)(Al,Si)O_3$ diamond inclusions, however, is inconsistent with our results. 

*Keywords:* perovskite; lower mantle; partitioning; oxygen; fugacity; diamond; ferric iron

## 1. Introduction

Magnesium silicate perovskite and magnesiowüstite are believed to comprise the bulk of Earth's lower mantle, along with a smaller quantity of calcium silicate perovskite. Changes in the

* Corresponding author. Tel.: +49-921-553737; Fax: +49-921-553769.
*E-mail address:* dan.frost@uni-bayreuth.de (D.J. Frost).

0012-821X/02/$ – see front matter 
PII: S0012-821X(02)00558-7

distribution of major elements between these phases as a function of either pressure, temperature or oxygen fugacity have the potential to significantly vary mineral compositions in the lower mantle and consequently affect physical and chemical properties. In particular, the way in which Fe, both ferrous and ferric, is partitioned between the dominant phases may influence lower mantle rheology and elasticity, in addition to transport properties such as electrical conductivity [1–3]. The 660 km seismic discontinuity, which marks the top of the lower mantle, is widely believed to result from the reaction of $(Mg,Fe)_2SiO_4$ ringwoodite to produce (Mg,Fe)O and (Mg,Fe)-$SiO_3$ perovskite [4]. The discontinuity appears to be very sharp requiring the reaction to take place over a narrow pressure interval. The partitioning of Fe between the phases involved will influence this interval and processes that affect the partitioning may therefore influence the sharpness of the discontinuity. Detailed information on the influence of pressure, temperature and composition on element partitioning at these conditions, therefore, allows important constrains to be placed on the nature of the mantle in this region. Recently it has been proposed that some rare inclusions found in diamonds may have formed in the lower mantle [5–7]. Although crystal structures unique to the lower mantle have not been preserved, the chemical compositions of $(Mg,Fe,Al)(Al,Si)O_3$, (Mg,Fe)O and $CaSiO_3$ inclusions appear to be consistent with very high-pressure formation. A comparison of partition coefficients between plausible coexisting pairs of inclusions with high-pressure experimental data not only allows a further test for ultra deep origin but may also provide additional information on the chemical and physical state of the lower mantle.

Given these wide implications a number of experimental studies have been performed to determine Fe–Mg partitioning between silicate perovskite and magnesiowüstite (see Fei [8] for review). Several studies, for example, have examined the effect of pressure on the Fe–Mg partitioning [9,10] and a dependence resulting from the perovskite $Al_2O_3$ content has also been observed [11,12]. In $Al_2O_3$-bearing systems there is a marked increase in the degree to which Fe partitions into perovskite. This observation is supported by Mössbauer spectroscopy measurements that show $Al_2O_3$-bearing perovskite to have a significantly greater $Fe^{3+}$ solubility than in the $Al_2O_3$-free system [13]. These observations are particularly relevant to the top of the lower mantle where garnet breaks down and the $Al_2O_3$ content of perovskite increases with pressure. Previous studies have also indicated that the high solubility of $Fe^{3+}$ in aluminous perovskite may also be independent of oxygen fugacity, requiring the lower mantle to contain significantly more $Fe^{3+}$ than the upper mantle [12,14]. However, other than demonstrating that $Al_2O_3$ has an effect, the quantitative dependence of the Fe–Mg partitioning on $Al_2O_3$ content cannot be discerned from these previous studies. Although the presence of $Al_2O_3$ apparently increases the maximum solubility of $Fe^{3+}$ in perovskite, it is unclear whether the effect on the Fe–Mg partitioning is solely a result of increased perovskite $Fe^{3+}$ content or if $Al_2O_3$ solubility also influences the $Fe^{2+}$ partitioning between the two phases.

Here we report a series of multianvil experiments performed in order to determine the precise effect of $Al_2O_3$ solubility in silicate perovskite on the Fe–Mg partitioning between this phase and magnesiowüstite. We have also been able to measure the $Fe^{3+}/\Sigma Fe$ ratio in coexisting perovskite and magnesiowüstite using electron energy-loss near-edge structure (ELNES) spectroscopy. We use these data to assess the likely mechanism for $Al^{3+}$ and $Fe^{3+}$ solubility in perovskite and compare our partitioning results with analyses of diamond inclusions, which are believed to have formed in the lower mantle.

## 2. Experimental methods

A suit of enstatite–ferrosilite compositions with Fe/(Fe+Mg) ratios of 0.05, 0.1, 0.15 and 0.3 (where Fe here and after refers to combined $Fe^{2+}$ and $Fe^{3+}$) were prepared from reagent grade oxides with Fe added as hematite. The oxides were ground together under alcohol, cold pressed into pellets and then fired in a $CO–CO_2$ gas mix furnace for 2 days at 1300°C at an oxygen fugac-

Table 1
Aluminous orthopyroxene starting compositions

| Comp | $SiO_2$ | FeO | MgO | $Al_2O_3$ | Si | Fe | Mg | Al | ΣCat | Fe/(Fe+Mg) |
|---|---|---|---|---|---|---|---|---|---|---|
| A10A | 53(1) | 3.3(2) | 33(1) | 9(1) | 0.91 | 0.05 | 0.86 | 0.18 | 2.00 | 0.05 |
| A10B | 51(2) | 6.3(3) | 31(1) | 9(1) | 0.89 | 0.09 | 0.82 | 0.20 | 2.00 | 0.1 |
| A10C | 53.8(7) | 8.9(6) | 31(2) | 7(1) | 0.93 | 0.13 | 0.81 | 0.14 | 2.01 | 0.14 |
| A10D | 52.6(4) | 14.4(7) | 27.5(9) | 6.3(6) | 0.93 | 0.21 | 0.73 | 0.13 | 2.00 | 0.23 |

Oxide analyses are reported in wt%. Numbers in brackets are 1 standard deviation on at least 20 microprobe analyses in terms of least units cited. Cations are reported normalised to three oxygens.

ity approximately 2 log units below the fayalite magnetite quartz buffer. The rapidly quenched samples were re-ground then re-fired at identical conditions for a further 3 days. X-ray diffraction of the recovered powders revealed no unreacted starting material. $Al_2O_3$-bearing pyroxenes containing approximately 10 wt% $Al_2O_3$ were prepared in a similar manner as for $Al_2O_3$-free pyroxene and were reduced in a gas mix furnace at identical conditions for similar lengths of time. These compositions were then placed in graphite capsules and sintered at 2.5 GPa and 1400°C for 3 days in a piston cylinder apparatus. Recovered compositions were analysed with X-ray diffraction and electron microprobe. The samples contained aluminous pyroxene with compositions given in Table 1. Two samples with higher Fe contents also contained minor amounts of garnet. Enstatite and aluminous enstatite compositions were then ground together with magnesiowüstite powders in the ratio one part magnesiowüstite to two parts enstatite, to give the starting compositions shown in Table 2. Some compositions were also ground together with 20 wt% metallic Fe to provide starting mixtures for experiments at more reducing conditions and in one experiment (H1717) starting powders were mixed with 30 wt% of a 1:1 Re and $ReO_2$ mixture.

Experiments were performed using a multianvil press and 10/4 and 7/3 octahedral pressure assemblies. The assemblies both use $LaCrO_3$ furnaces. Capsules of Re metal were spark eroded with four sample chambers. In the 7/3 assembly two capsules could be placed on either side of the thermocouple which was inserted axially through the wall of the furnace. Experiments were run for between 1 h and 1 day at temperatures of 1650 and 1900°C and pressures between 24 and 25 GPa. The recovered samples were mounted in epoxy resin and polished for analysis with electron microprobe and phase identification by Raman spectroscopy.

Two samples (H1495a and -b) were also made into petrographic thin sections for analytical transmission electron microscopy (TEM). These sections were glued on 3 mm diameter copper grids and then thinned to electron-transparency

Table 2
Fe/(Fe+Mg) ratios of starting materials

| Alumina-free compositions | | | Alumina-bearing compositions | | |
|---|---|---|---|---|---|
| | orthopyroxene | magnesiowüstite | | orthopyroxene | magnesiowüstite |
| AB | 0.05 | 0.1 | A | 0.05 (A10A) | 0.1 |
| A | 0.05 | 0.2 | B | 0.05 (A10A) | 0.4 |
| B | 0.05 | 0.4 | D | 0.1 (A10B) | 0.2 |
| C | 0.1 | 0.2 | E | 0.14 (A10C) | 0.2 |
| D | 0.1 | 0.6 | F | 0.23 (A10D) | 0.4 |
| E | 0.15 | 0.4 | | | |
| F | 0.15 | 0.8 | | | |

Fe/(Fe+Mg) ratios are reported for each phase. The labels in brackets refer to the orthopyroxene analyses given in Table 1.

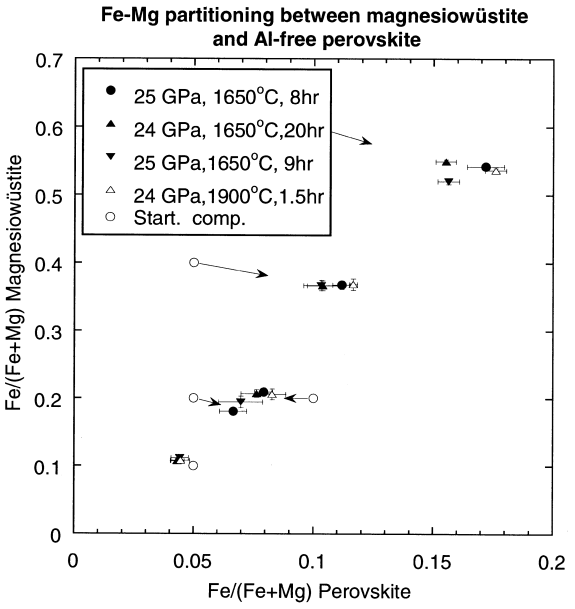


Fig. 1. The Fe/(Fe+Mg) molar ratios (where $Fe = Fe^{2+} + Fe^{3+}$) of perovskite versus magnesiowüstite from $Al_2O_3$-free experiments performed in Re metal capsules. Error bars are 1 σ from at least 20 pairs of microprobe analyses.

by argon ion bombardment in a Gatan DUO-MILL machine. To avoid amorphisation of silicate perovskite, thinning was done under liquid nitrogen cooling and at low-acceleration voltage (3 kV) and beam current (0.5 mA). Textures and defect microstructures of samples were observed in a PHILIPS CM20 FEG (field emission gun) STEM operating at 200 kV. Compositions of coexisting magnesiowüstite and perovskite grains were measured with a ThermoNoran Vantage energy-dispersive (EDX) system equipped with a Norvar ultra-thin window and a germanium detector. The quantification of EDX microanalyses was performed according to the method of Van Cappellen and Doukhan [15], and corrected for X-ray absorption on the basis of the principle of electro-neutrality.

The same grains were also analysed for $Fe^{3+}/\Sigma Fe$ using the attached Gatan PEELS 666 (parallel electron energy-loss spectrometer). The determination of the $Fe^{3+}/\Sigma Fe$ ratio is based on the white line intensities at the Fe $L_{23}$ edge; these intensities have been calibrated for minerals in the high-spin state [16]. Fe $L_{23}$ ELNES spectra were measured in diffraction mode with convergence and collection semi-angles of $\alpha = 8$ mrad and $\beta = 2.7$ mrad and an energy dispersion of 0.1 eV per channel. The energy resolution, measured as width of the zero-loss peak at half maximum, was ca. 0.8–0.9 eV. To improve the counting statistics and to check for possible beam-induced oxidation, six spectra were measured in a time series with integration times of 10–20 s each. Spectra were then corrected for dark current and channel-to-channel gain variation. To extract the pure single-scattering core-loss signal an inverse power-law background was subtracted and multiple-scattering contributions were removed by the Fourier-ratio technique [17]. Errors in the $Fe^{3+}/\Sigma Fe$ ratio are usually estimated to be 0.05 but for samples with low Fe contents ($< 3$ wt%) uncertainties are larger (i.e. 0.08) due to the limited counting statistics.

## 3. Partitioning results and TEM observations

Results from partitioning experiments performed in Re capsules in the $Al_2O_3$-free system (Fig. 1) show that Fe partitions more favourably into magnesiowüstite than perovskite under these conditions. The chemical compositions of the phases from experiments where equilibrium was considered to have been achieved are given in Table 3. The intention was to approach equilibrium from both Fe-rich and Fe-poor starting compositions, however, perovskite starting mixtures with $Fe/(Fe+Mg) > 0.1$ consistently broke down to form magnesiowüstite and stishovite such that true reversals were only successful at low Fe/(Fe+Mg) ratios. In order to demonstrate equilibrium we performed a time study at 1650°C, the results of which are shown in Fig. 2. The apparent Fe–Mg distribution coefficient, or $K^{app}$, which includes $Fe^{3+}$, is defined in a similar way to Wood [18]:

$$K^{app} = \frac{X_{Fe}^{Pv} X_{Mg}^{Mw}}{X_{Mg}^{Pv} X_{Fe}^{Mw}} \quad (1)$$

Table 3
Phase compositions in the $Al_2O_3$-free system

| Run number, start comp., *P*, *T*, run time | | Chemical composition in atoms per formula unit | | | | | |
|---|---|---|---|---|---|---|---|
| | | Si | Mg | ΣFe | ΣCat | ΣFe/(ΣFe+Mg) | $Fe^{3+}$/ΣFe |
| H1472, 25GPa, 1650°C, 8 h | | | | | | | |
| A | Pv | 0.978(7) | 0.974(15) | 0.070(6) | 2.022 | 0.067(6) | |
| | Mw | 0.001(2) | 0.818(3) | 0.180(3) | 0.999 | 0.181(3) | |
| D | Pv | 0.97(2) | 0.878(36) | 0.182(7) | 2.030 | 0.172(8) | |
| | Mw | 0.001(1) | 0.458(4) | 0.542(4) | 1.000 | 0.542(4) | |
| C | Pv | 0.976(7) | 0.963(16) | 0.083(3) | 2.023 | 0.079(4) | |
| | Mw | 0.001(2) | 0.791(3) | 0.209(3) | 1.000 | 0.209(3) | |
| B | Pv | 0.970(8) | 0.941(14) | 0.118(4) | 2.030 | 0.112(4) | |
| | Mw | 0.001(1) | 0.632(6) | 0.367(6) | 1.000 | 0.367(6) | |
| V135a, 24 GPa, 1650°C, 20 h | | | | | | | |
| AB | Pv | 0.973(11) | 1.008(22) | 0.046(3) | 2.027 | 0.043(3) | |
| | Mw | 0.001(1) | 0.891(3) | 0.107(3) | 0.999 | 0.107(3) | |
| B | Pv | 0.974(12) | 0.943(26) | 0.109(6) | 2.026 | 0.104(6) | |
| | Mw | 0.002(1) | 0.631(7) | 0.365(7) | 0.998 | 0.366(7) | |
| C | Pv | 0.972(6) | 0.974(14) | 0.081(7) | 2.028 | 0.076(7) | |
| | Mw | 0.001(1) | 0.791(6) | 0.206(5) | 0.999 | 0.207(5) | |
| D | Pv | 0.957(10) | 0.917(16) | 0.168(6) | 2.043 | 0.155(4) | |
| | Mw | 0.004(2) | 0.447(3) | 0.545(3) | 0.996 | 0.550(3) | |
| H1495a, 25 GPa, 1650°C, 9 h | | | | | | | |
| AB | Pv | 0.981(20) | 0.991(36) | 0.046(5) | 2.018 | 0.044(4) | 0.084(50) |
| | Mw | 0.001(1) | 0.888(3) | 0.112(3) | 1.000 | 0.112(3) | 0.000(50) |
| B | Pv | 0.979(12) | 0.934(23) | 0.107(8) | 2.020 | 0.103(7) | 0.237(50) |
| | Mw | 0.001(1) | 0.632(8) | 0.366(8) | 0.999 | 0.367(8) | 0.114(50) |
| A | Pv | 0.973(22) | 0.980(34) | 0.074(13) | 2.027 | 0.070(9) | 0.085(50) |
| | Mw | 0.000(1) | 0.805(8) | 0.194(9) | 1.000 | 0.195(9) | 0.189(50) |
| D | Pv | 0.964(11) | 0.904(18) | 0.167(7) | 2.036 | 0.156(5) | 0.247(50) |
| | Mw | 0.003(5) | 0.477(6) | 0.517(7) | 0.997 | 0.520(4) | 0.071(50) |
| S2676, 24 GPa, 1900°C, 1.5 h | | | | | | | |
| D | Pv | 0.963(11) | 0.885(21) | 0.189(3) | 2.037 | 0.176(4) | |
| | Mw | 0.001(1) | 0.463(3) | 0.536(3) | 0.999 | 0.537(3) | |
| AB | Pv | 0.979(8) | 0.995(17) | 0.046(4) | 2.021 | 0.045(4) | |
| | Mw | 0.001(1) | 0.892(1) | 0.108(1) | 1.000 | 0.108(1) | |
| B | Pv | 0.98(1) | 0.919(17) | 0.121(3) | 2.020 | 0.116(2) | |
| | Mw | 0.000(1) | 0.631(8) | 0.368(8) | 1.000 | 0.368(8) | |
| C | Pv | 0.981(7) | 0.953(16) | 0.086(6) | 2.019 | 0.083(6) | |
| | Mw | 0.001(1) | 0.794(8) | 0.206(8) | 1.000 | 0.206(8) | |

All runs were performed in Re capsules. Starting composition letters refer to those given Table 2. All Fe (ΣFe) is treated as FeO. Electron microprobe analyses were performed using a Cameca SX-50 operating at 15 kV and 5 nA. Standards were $MgSiO_3$ glass for Mg, andradite for Si, spinel for Al and Fe metal. The data were reduced using the PAP correction routine. The numbers in brackets are 1 standard deviation on at least 20 microprobe analyses in terms of least units cited. $Fe^{3+}$/ΣFe uncertainties are 1 standard deviation from two to three analyses or 5% where only one analysis was made.

where

$$X_{Fe}^{Pv} = \frac{Fe^{2+} + Fe^{3+}}{Fe^{2+} + Fe^{3+} + Mg^{2+}} \quad (2)$$

$K^{app}$ increases with time to a plateau at around 8 h. Therefore, we believe experiments performed for 8 h or longer should be at or very close to equilibrium for this temperature. TEM observations also support that equilibrium has been

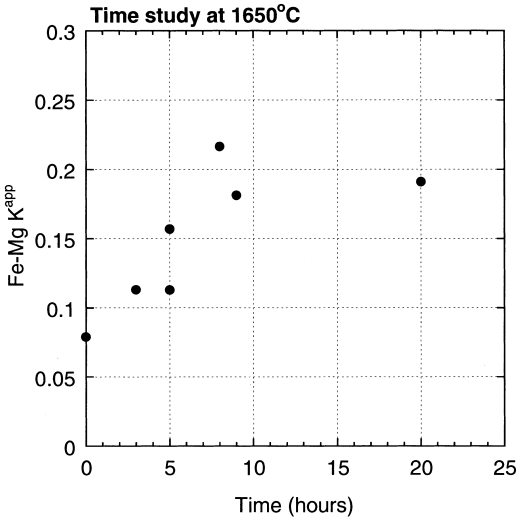


Fig. 2. A time study performed in Re capsules at 24 GPa and 1650°C in the $Al_2O_3$-free system using starting composition B given in Table 2. $K^{app}$ is defined as $(Fe/Mg)_{Pv}/(Fe/Mg)_{Mw}$ where $Fe = Fe^{2+}+Fe^{3+}$. $K^{app}$ increases with time but reaches a plateau at around 8 h.

achieved. Both $Al_2O_3$-free and $Al_2O_3$-bearing samples show equilibrium textures, with equant grains meeting at angles close to the optimum 120° angle (Fig. 3a,b). Silicate perovskite is absolutely defect-free, whereas the softer magnesiowüstite grains contain very few dislocations.

Results from experiments performed in the $Al_2O_3$-bearing system are shown in Fig. 4. In these experiments a three-phase assemblage of garnet, aluminous perovskite and magnesiowüstite was observed. The compositions of these phases are reported in Table 4. With increasing pressure the $Al_2O_3$ content of both perovskite and garnet increased in line with previous observations in the $MgSiO_3$–$Mg_3Al_2Si_3O_{12}$ system [19]. The perovskite $Al_2O_3$ contents vary between approximately 4 and 7 wt%, or 0.1–0.16 atoms per $MgSiO_3$ formula unit, over the pressure range. As the $Al_2O_3$ content of perovskite increases with pressure, the molar Fe/(Fe+Mg) ratio of perovskite increases relative to the magnesiowüstite Fe/(Fe+Mg) ratio. A clear correlation can be observed in our results between the perovskite $Al_2O_3$ content and the Fe distribution. This is demonstrated in Fig. 5 where the Al content, in formula units, is shown above each data point with a parameterisation of these results contoured for the perovskite Al content. The parameterisation was performed by first fitting the $Al_2O_3$-free data to a thermodynamic expression describing the free energy change of the ion exchange reaction. The ion exchange reaction for the partitioning is:

$$FeSiO_{3\,perovskite} + \underset{magnesiowüstite}{MgO} = MgSiO_{3\,perovskite} + \underset{magnesiowüstite}{FeO} \quad (3)$$

$K^{app}$ for this reaction, as defined in Eq. 1), can be written in terms of two interaction parameters and the standard state free energy change of Eq. 3:

$$RT\ ln\ K^{app} = -\Delta G^0_{(3)} + W^{Pv}_{FeMg}(2\,X^{Pv}_{Fe}-1)+ W^{Mw}_{FeMg}(1-2\,X^{Mw}_{Fe}) \quad (4)$$

The full derivation of this equation can be found in Matsuzaka et al. [20]. Least squares fitting of Eq. 4 to the $Al_2O_3$-free data gives $\Delta G^0 = 24500$ J/mol, $W^{Pv}_{FeMg} = 1650$ J/mol, and $W^{Mg}_{FeMg} = 12000$ J/mol at 1650°C. We treat here all Fe as FeO, so the parameters are not strictly thermodynamically

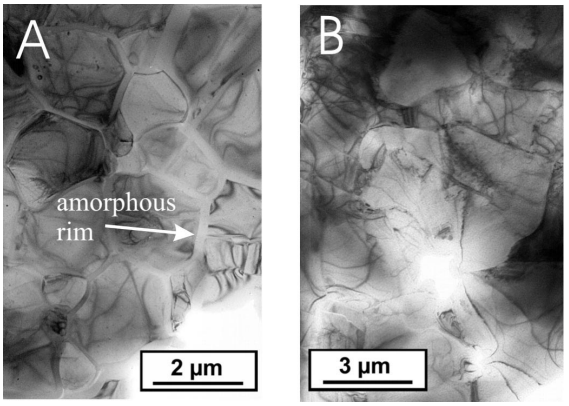


Fig. 3. Bright field TEM images of equilibrated samples showing coexisting perovskite and magnesiowüstite in $Al_2O_3$-free (A) and $Al_2O_3$-bearing (B) systems. Amorphous rims can be seen around the more beam-sensitive $Al_2O_3$-free perovskites in (A) but not in the $Al_2O_3$-bearing system. Note 120° triple junctions and the lack of metallic Fe that would indicate disproportionation of $Fe^{2+}$. Light areas in (B) are holes produced from ion thinning.

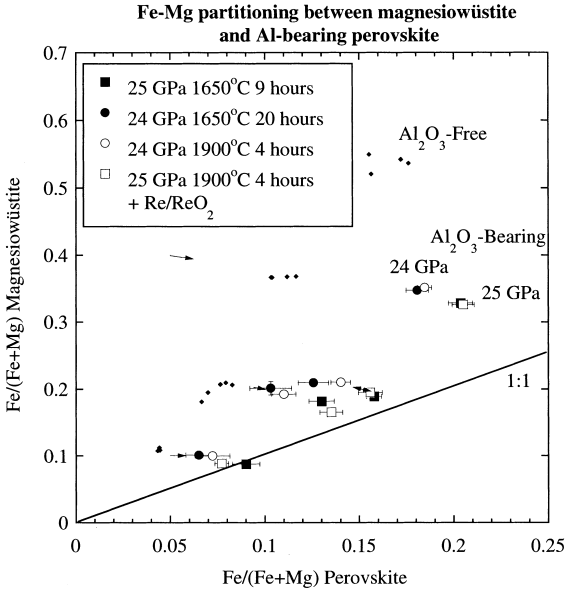


Fig. 4. The Fe/(Fe+Mg) molar ratios of perovskite and magnesiowüstite from $Al_2O_3$-bearing experiments performed in Re metal capsules with all Fe reported as FeO. The $Al_2O_3$-content of perovskite increases with pressure from approximately 4 to 7 wt% between 24 and 25 GPa. All samples coexisted with garnet. The arrows denote the starting compositions and the direction of approach to equilibrium. The results from $Al_2O_3$-free experiments are shown for comparison.

valid. Then, at fixed values of $X_{Fe}^{Mw}$ we define the $Al_2O_3$-bearing perovskite Fe/(Fe+Mg) ratio ($X_{Fe}^{Al-Pv}$) as a function of Al content, in $MgSiO_3$ formula units, using the equation:

$$X_{Fe}^{Al-Pv} = X_{Fe}^{Pv} + \alpha Al^2 \quad (5)$$

where $X_{Fe}^{Pv}$ is the Fe/(Fe+Mg) ratio for $Al_2O_3$-free perovskite, which is calculated at a given $X_{Fe}^{Mw}$ from Eq. 4. The coefficient was determined by a weighted least squares regression to both $Al_2O_3$-free and $Al_2O_3$-bearing data to give $\alpha = 3.67$. A non-linear dependence on the Al content was required to adequately fit the data. The treatment of Al here is purely empirical so the values obtained have no thermodynamic significance and are used here only to describe the current results. It can be seen in Fig. 5 that the results of experiment H1717, where Re and $ReO_2$ were added to the starting compositions, are quite consistent with the other experiments where $ReO_2$ was not present.

Several previous studies have shown that the presence of $Al_2O_3$ influences the solubility of $Fe^{3+}$ in perovskite [13,14]. In our results described so far no distinction has been made between $Fe^{2+}$ and $Fe^{3+}$, however, in Tables 3 and 4 $Fe^{3+}/\Sigma Fe$ ratios of coexisting magnesiowüstite and perovskite crystals are reported from ELNES spectroscopic analyses. Perovskite is known to become rapidly amorphous under the TEM electron beam. This effect was particularly obvious for the $Al_2O_3$-free perovskite (Fig. 3a), whereas $Al_2O_3$-bearing perovskite turned out to be distinctly less beam-sensitive. The amorphisation is commonly accompanied by Fe oxidation and a loss in sharpness of the white lines. A time series of spectra were recorded that enabled oxidation to be recognised and then minimised by adjusting the illumination conditions. Typical ELNES spectra for magnesiowüstite and perovskite produced in the $Al_2O_3$-free and -bearing systems are shown in Fig. 6. While the presence of $Al_2O_3$ does not

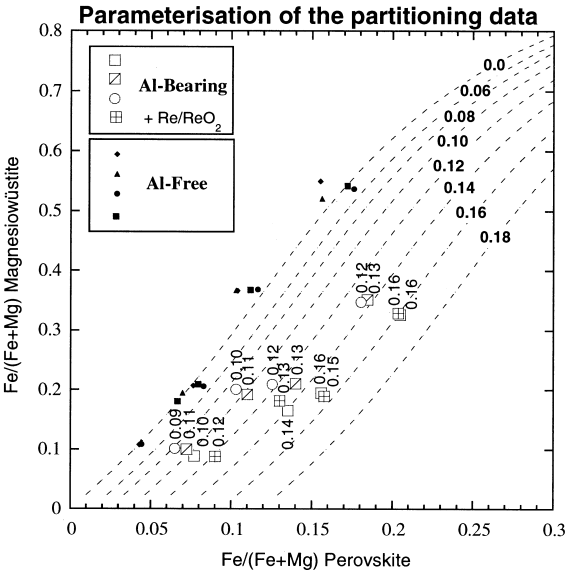


Fig. 5. The $Al_2O_3$-free and $Al_2O_3$-bearing results are shown with the Al content of perovskite, in atoms per formula unit normalised to two cations, above each data point. A parameterisation of the Fe–Mg partitioning data is shown with contours for the Al content of perovskite.

Table 4
Phase compositions in the $Al_2O_3$-bearing system

| Run number, start comp. | | Chemical composition in atoms per formula unit | | | | | | |
|---|---|---|---|---|---|---|---|---|
| | | Si | Mg | ΣFe | Al | ΣCat | ΣFe/(ΣFe+Mg) | $Fe^{3+}$/ΣFe |
| V135b, 24GPa, 1650°C, 20 h | | | | | | | | |
| A | Gt | 3.368(53) | 3.150(46) | 0.196(9) | 1.28(73) | 7.993 | 0.059(3) | |
| | Pv | 0.926(11) | 0.946(17) | 0.066(6) | 0.090(14) | 2.029 | 0.065(7) | |
| | Mw | 0.001(1) | 0.891(3) | 0.100(3) | 0.0040(1) | 0.997 | 0.101(3) | |
| D | Gt | 3.531(40) | 3.046(79) | 0.359(11) | 1.021(97) | 7.958 | 0.105(5) | |
| | Pv | 0.928(18) | 0.881(24) | 0.101(9) | 0.107(28) | 2.018 | 0.103(11) | |
| | Mw | 0.004(13) | 0.788(23) | 0.198(6) | 0.003(2) | 0.994 | 0.201(10) | |
| E | Gt | 3.08(9) | 2.69(15) | 0.386(42) | 1.84(16) | 8.001 | 0.125(19) | |
| | Pv | 0.91(1) | 0.871(19) | 0.125(7) | 0.122(20) | 2.029 | 0.126(8) | |
| | Mw | 0.001(1) | 0.786(3) | 0.207(3) | 0.0030(3) | 0.998 | 0.209(3) | |
| B | Gt | 3.324(45) | 2.906(59) | 0.531(20) | 1.275(77) | 8.038 | 0.155(8) | |
| | Pv | 0.877(5) | 0.868(11) | 0.191(6) | 0.124(9) | 2.061 | 0.181(6) | |
| | Mw | 0.002(3) | 0.646(5) | 0.344(3) | 0.003(1) | 0.996 | 0.347(4) | |
| H1495b, 25GPa, 1650°C, 9 h | | | | | | | | |
| A | Gt | 3.249(72) | 3.076(93) | 0.174(6) | 1.502(78) | 8.001 | 0.054(2) | |
| | Pv | 0.905(12) | 0.919(11) | 0.088(8) | 0.122(17) | 2.034 | 0.087(8) | 0.76(11) |
| | Mw | 0.001(2) | 0.900(3) | 0.087(2) | 0.007(1) | 0.995 | 0.088(1) | 0.001(8) |
| D | Gt | 3.310(46) | 2.949(29) | 0.323(14) | 1.404(87) | 7.987 | 0.099(3) | |
| | Pv | 0.902(7) | 0.881(9) | 0.126(7) | 0.127(15) | 2.035 | 0.125(7) | 0.82(8) |
| | Mw | 0.001(1) | 0.810(3) | 0.180(2) | 0.006(1) | 0.996 | 0.181(2) | 0.09(8) |
| E | Gt | 3.01(2) | 2.80(17) | 0.365(49) | 1.88(14) | 8.052 | 0.116(16) | |
| | Pv | 0.878(7) | 0.856(12) | 0.160(4) | 0.152(5) | 2.046 | 0.157(4) | 0.67(5) |
| | Mw | 0.0010(2) | 0.802(2) | 0.187(2) | 0.0060(3) | 0.996 | 0.189(2) | 0.07(5) |
| B | Gt | 3.227(27) | 2.814(29) | 0.48(3) | 1.50(5) | 8.023 | 0.146(8) | 0.20(5) |
| | Pv | 0.870(6) | 0.815(7) | 0.208(7) | 0.158(6) | 2.051 | 0.204(6) | 0.68(5) |
| | Mw | 0.001(1) | 0.664(4) | 0.324(3) | 0.006(1) | 0.996 | 0.328(3) | 0.19(5) |
| S2705, 24 GPa, 1900°C, 4 h | | | | | | | | |
| A | Gt | 3.44(11) | 3.14(22) | 0.193(23) | 1.18(32) | 7.963 | 0.058(3) | |
| | Pv | 0.922(10) | 0.919(9) | 0.07(1) | 0.110(18) | 2.023 | 0.072(9) | |
| | Mw | 0.002(2) | 0.885(5) | 0.098(2) | 0.009(1) | 0.994 | 0.100(3) | |
| D | Gt | 3.369(55) | 3.01(5) | 0.314(9) | 1.29(11) | 7.985 | 0.094(2) | |
| | Pv | 0.917(10) | 0.888(16) | 0.109(6) | 0.110(17) | 2.027 | 0.110(6) | |
| | Mw | 0.003(6) | 0.793(10) | 0.188(4) | 0.008(1) | 0.993 | 0.192(3) | |
| E | Gt | 3.19(12) | 2.84(11) | 0.352(14) | 1.60(25) | 8.000 | 0.110(4) | |
| | Pv | 0.898(6) | 0.866(7) | 0.137(5) | 0.134(7) | 2.035 | 0.137(5) | |
| | Mw | 0.004(9) | 0.775(14) | 0.206(5) | 0.007(1) | 0.992 | 0.210(2) | |
| B | Gt | 3.296(30) | 2.78(2) | 0.522(9) | 1.340(44) | 8.003 | 0.158(3) | |
| | Pv | 0.894(3) | 0.826(5) | 0.187(4) | 0.133(3) | 2.040 | 0.184(4) | |
| | Mw | 0.003(2) | 0.638(4) | 0.345(3) | 0.008(1) | 0.994 | 0.351(2) | |
| H1717, 25 GPa, 1900°C, 4 h with added $ReO_2$ | | | | | | | | |
| D | Gt | 3.21(1) | 3.09(1) | 0.224(7) | 1.510(5) | 8.040 | 0.068(2) | |
| | Pv | 0.890(6) | 0.871(8) | 0.136(6) | 0.142(8) | 2.039 | 0.135(6) | |
| | Mw | 0.001(1) | 0.822(5) | 0.162(4) | 0.008(1) | 0.994 | 0.165(4) | |
| B | Gt | 3.30(2) | 2.92(6) | 0.46(2) | 1.34(2) | 8.030 | 0.137(4) | |
| | Pv | 0.864(6) | 0.812(5) | 0.209(7) | 0.167(6) | 2.053 | 0.205(6) | |
| | Mw | 0.002(1) | 0.661(3) | 0.320(4) | 0.010(1) | 0.993 | 0.326(4) | |
| A | Gt | 3.26(2) | 3.15(4) | 0.145(9) | 1.45(4) | 8.010 | 0.044(3) | |
| | Pv | 0.916(6) | 0.941(6) | 0.079(4) | 0.100(6) | 2.035 | 0.077(4) | |
| | Mw | 0.002(3) | 0.897(6) | 0.087(2) | 0.008(1) | 0.994 | 0.088(2) | |
| E | Pv | 0.870(5) | 0.853(6) | 0.157(7) | 0.166(4) | 2.047 | 0.156(6) | |
| | Mw | 0.001(1) | 0.795(3) | 0.192(3) | 0.007(1) | 0.995 | 0.194(3) | |

Legend as in Table 3.

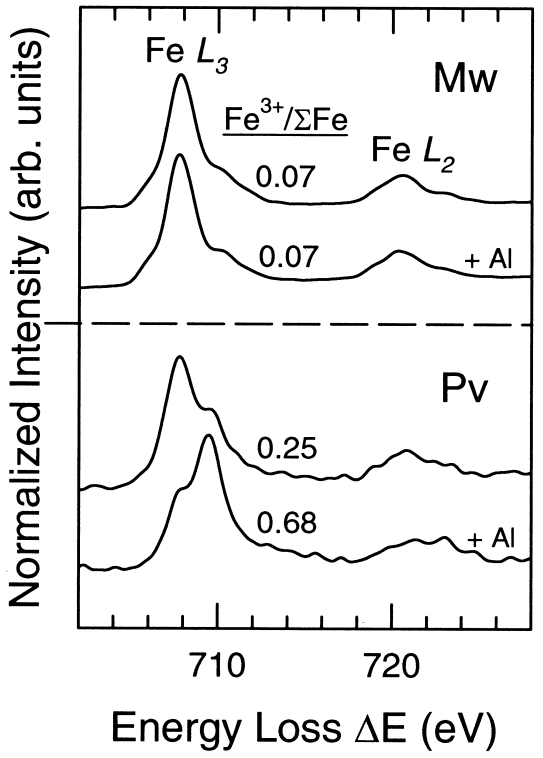


Fig. 6. Typical Fe $L_{23}$ ELNES of magnesiowüstite (Mw) and perovskite (Pv) in $Al_2O_3$-free and -bearing (+Al) systems. The spectra have been normalised to their maximum intensity and shifted vertically for clarity. Note the variation in the intensity of the peaks at 707.8 and 709.5 eV, reflecting the variation in the $Fe^{2+}$ and $Fe^{3+}$ contents, respectively. Spectra have been gain-normalised, background-subtracted and deconvoluted using the low-loss spectra and the $Fe^{3+}/\Sigma Fe$ ratio has been determined by the treatment described by van Aken et al. [16].

apparently affect the spectra for magnesiowüstite, the white line intensities at the $L_3$ edge are obviously influenced by the incorporation of $Al_2O_3$ in perovskite. The peak intensity of the $L_3$ edge shows a chemical shift to higher energy in the $Al_2O_3$-bearing perovskite reflecting a much higher $Fe^{3+}/\Sigma Fe$ ratio [16]. Fig. 7 shows analyses of magnesiowüstite and perovskite $Fe^{3+}/\Sigma Fe$ ratios from experiment H1495 in both $Al_2O_3$-free and $Al_2O_3$-bearing systems, plotted against the Fe/(Fe+Mg) ratio of the particular phase. For magnesiowüstite in both systems the $Fe^{3+}/\Sigma Fe$ ratios increase with Fe/(Fe+Mg) but do not exceed 20%. These results are in agreement with several previous studies on magnesiowüstite $Fe^{3+}/\Sigma Fe$ ratios at high pressure [21,22]. In the $Al_2O_3$-free system, the perovskite $Fe^{3+}/\Sigma Fe$ ratio also increases with Fe/(Fe+Mg) ratio to reach a maximum of approximately 20%. $Al_2O_3$-bearing perovskite $Fe^{3+}/\Sigma Fe$ ratios, however, are over three times greater, falling between 60 and 80%. Although we are not able to demonstrate equilibrium for the $Fe^{3+}$ concentrations, we note that in a previous study [14] oxidation of $Fe^{2+}$ in perovskite from initially reduced starting compositions occurred very rapidly, resulting in $Fe^{3+}/\Sigma Fe$ ratios of 30% in 1 h and similar ratios after 8 h.

## 4. Partitioning under more reducing conditions

Partitioning experiments attempted under reducing conditions, in the presence of metallic Fe, were hindered by several problems. Initially, multi-chamber Fe capsules were employed to impose reducing conditions but these were discarded after it was found that the junction between the Fe capsule and the outer MgO sleeve of the multi-

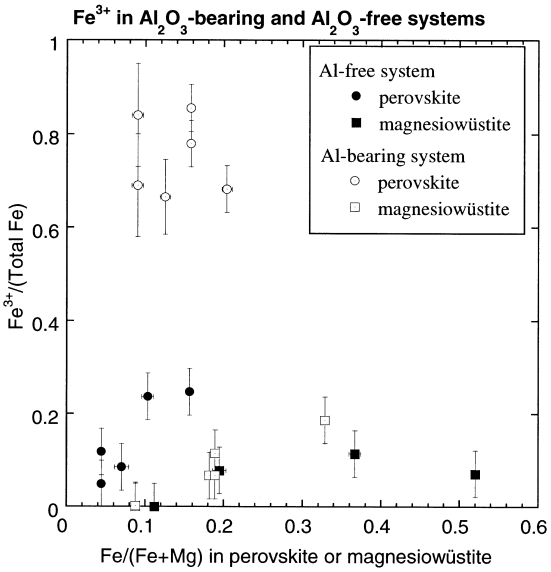


Fig. 7. ELNES spectroscopic measurements of $Fe^{3+}/\Sigma Fe$ ratios for coexisting magnesiowüstite and perovskite in $Al_2O_3$-free (filled symbols) and $Al_2O_3$-bearing (open symbols) systems from experiment H1495.

anvil assembly imposes a very low $fO_2$ on the samples. This results in metallic Fe precipitation mainly from the magnesiowüstite within the samples. The precipitation of Fe metal from magnesiowüstite is a relatively slow process and for phases where Fe–Mg equilibrium is achieved rapidly, such as for ringwoodite and magnesiowüstite [22], this does not pose a significant problem. Although some reduction may take place the Fe–Mg equilibrium between the phases is still maintained. For perovskite and magnesiowüstite, on the other hand, the attainment of Fe–Mg equilibrium takes much longer in comparison to the much faster reduction of FeO, such that almost all the FeO is reduced out of magnesiowüstite before the perovskite Fe/(Fe+Mg) ratio has shifted even slightly towards equilibrium.

A number of further experiments were then performed using alumina capsules with 20 wt% metallic Fe added to the starting mixtures. Experiments in both $Al_2O_3$-free and $Al_2O_3$-bearing systems performed for over 1 day at 1650°C and 25 GPa, however, showed no noticeable shift in composition from the starting Fe/(Fe+Mg) ratios. The relatively low $fO_2$ most likely reduces the point defect concentration within perovskite and significantly reduces the rate of cation diffusion. We estimate that to reach Fe–Mg equilibrium between perovskite and magnesiowüstite requires at least one order of magnitude more time at metallic Fe saturation than under more oxidising conditions in Re capsules, for grain sizes analysable with the electron microprobe ($\geq 5$ μm).

## 5. Discussion

The high $Fe^{3+}/\Sigma Fe$ ratios measured for $Al_2O_3$-bearing perovskite in this study seem to imply that these samples were synthesised at relatively oxidising conditions. The first question to address, therefore, is from where does the additional oxygen in these products originate? The starting materials were all synthesised under reducing conditions and in only one experiment (H1717) was an additional oxidant ($ReO_2$) added to the sample. It has been suggested that the high $Fe^{3+}$ concentrations measured in $Al_2O_3$-bearing perovskite might result from disproportionation of $Fe^{2+}$ to produce metallic Fe and $Fe^{3+}$ [14]. TEM investigation, however, did not detect any metallic Fe within our samples, as seen in Fig. 3a,b, so in this case we can discount this mechanism. There are, however, a number of possible sources of oxidant in such multianvil experiments. Pore space oxygen, for example, may be relatively high in these samples because they are small and the powders are difficult to pack down to a high density. Similarly, $H_2O$ in the assembly could also oxidise the sample or connect relatively oxidised regions of the assembly, such as the $LaCrO_3$ furnace, with the sample. The MgO sleeve adjacent to the furnace contains up to 2 wt% Cr after the experiments. If Cr is in the 2+ valence state in the MgO, as seems plausible judging from a previous study [23], the reduction of the $Cr^{3+}$ from the furnace would release a significant amount of oxygen. As the additional oxygen did not arise from the starting material itself, one of these aforementioned external sources must be responsible for the oxidation. The system must therefore be open with respect to oxygen in this type of multianvil configuration.

In experiment H1717 30 wt% of a Re–$ReO_2$ mix was added to the starting compositions. After the experiment scanning electron microscopy and electron microprobe analyses revealed Re and $ReO_2$ dispersed throughout the samples in the approximate proportions to which they were added. The partitioning results from this experiment are identical to the other Al-bearing experiments where $ReO_2$ was not added, within the experimental uncertainties. This implies that either all the experiments run in Re capsules experienced an oxygen fugacity indistinguishable from the Re–$ReO_2$ buffer, whether $ReO_2$ was added or not, or that the oxygen fugacity has little influence on the observed partitioning. We find the former scenario to be more likely. The fact that the quantities of the buffering assemblage were not perturbed significantly during the experiment is a good indication that the ambient oxygen fugacity of the multianvil assembly is close to Re–$ReO_2$, even in the absence of $ReO_2$.

When we compare our $Al_2O_3$-free results with previously published partitioning data collected at similar conditions [8] we find that these studies

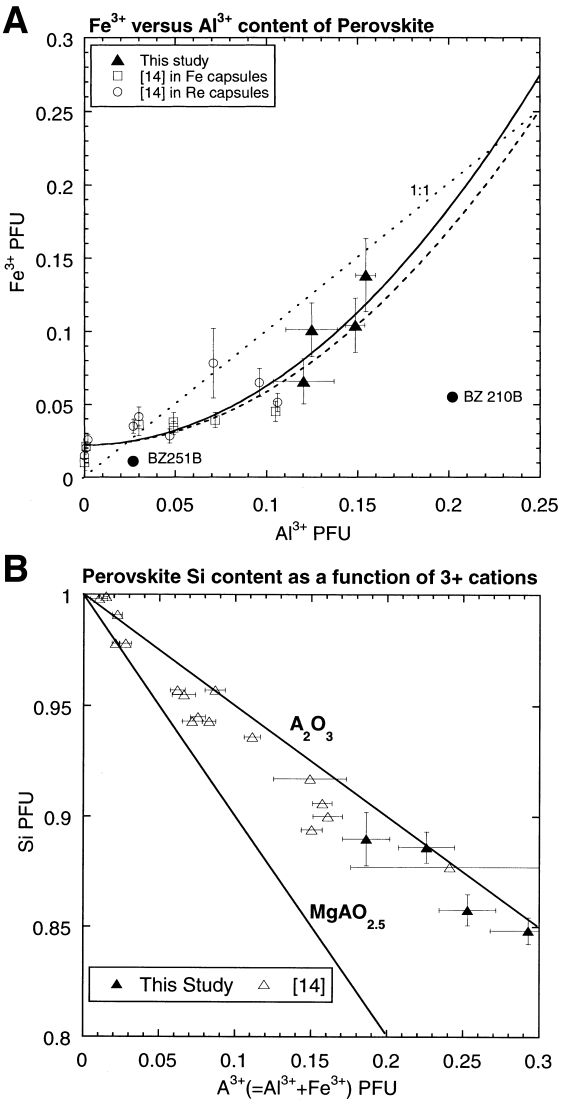


Fig. 8. (A) The variation of Al and $Fe^{3+}$ in silicate perovskite reported as atoms per formula unit (PFU) normalised to two cations. Results are from this study and that of Lauterbach et al. [14]. The dotted line shows a 1:1 correspondence. The solid curve is a least squares regression to both data sets. The dashed curve shows the dependence of the perovskite Fe/(Fe+Mg) ratio with $Al_2O_3$ concentration determined from Eq. 5 of the partitioning parameterisation. The compositions of two $(Mg,Fe,Al)(Al,Si)O_3$ diamond inclusions from San Luiz are also shown [6]. (B) The variation of the Si content of perovskite with combined 3+ atoms (i.e. $A^{3+} = Al^{3+}+Fe^{3+}$). Two curves for likely substitution mechanisms are indicated. For the component $A_2O_3$ substitution of $A^{3+}$ cations takes place onto both six-fold and eight-fold sites, while for the $MgAO_{2.5}$ component $A^{3+}$ cations are only on the six-fold site balanced by an oxygen vacancy.

mainly report lower values for the apparent distribution coefficient, $K^{app}$ as defined in Eq. 1, than observed in our experiments. It is quite likely, however, that equilibrium was not reached in many previous studies because run times were generally less than 1 h. The only previously published $Al_2O_3$-free results to be in good agreement with our data are those of Katsura and Ito [24], who used a $B_2O_3$ flux to aid the attainment of equilibrium. For the $Al_2O_3$-bearing system we also find a poor agreement between our parameterised results and those previously reported [11,12,25]. Although clearly an effect on the partitioning can be observed due to the presence of $Al_2O_3$ in these studies, no quantitative trend with the perovskite $Al_2O_3$ content is observed when these data are considered, even allowing for the fact that $fo_2$ may also influence partitioning. We can only conclude that equilibrium was not fully achieved in many of these previous experiments as run times were again comparatively short and in the range 0.3–4 h.

In Fig. 8a the concentrations of Al and $Fe^{3+}$ in perovskite samples are plotted from this study along with those of Lauterbach et al. [14]. In the study of Lauterbach et al. the capsule material used does not appear to have influenced the reported $Fe^{3+}$ contents. The similarity in $Fe^{3+}$ contents measured in both Fe and Re capsules could mean that either the perovskite $Fe^{3+}$ concentration is independent of oxygen fugacity or that the use of Fe capsules alone was not effective in buffering the oxygen fugacity of the entire sample. Either way, the results from both capsule types used by Lauterbach et al. and our results form a consistent trend with the Al content. Such a trend would probably not be observed if $Fe^{3+}$ were not saturated in the perovskite structure for a given Al concentration.

When our results and those of Lauterbach et al. [14] are considered together in Fig. 8a the $Fe^{3+}$ concentration has an apparently non-linear dependence on the Al content. For low Al contents the $Fe^{3+}$ dependence is relatively weak and might be considered linear, but as the Al contents rise above 0.1 formula units the gradient increases and compositions containing equal Al and $Fe^{3+}$ are approached. While the solid curve in Fig. 8a is

a least squares fit to the two data sets, the dashed curve is taken from Eq. 5 of the Fe–Mg partitioning parameterisation. Eq. 5 gives the variation in Fe/(Fe+Mg) ratio of $Al_2O_3$-bearing perovskite, as a function of the Al content, at a fixed magnesiowüstite Fe content. The intercept on the *y*-axis of the dashed curve was adjusted to correspond to the average $Fe^{3+}$ content of Al-free perovskite. In reality this intercept will vary as a function of the perovskite Fe/(Fe+Mg) ratio as indicated in Fig. 7 but because this effect is much smaller than the influence of Al we have ignored it here. The two curves shown in Fig. 8a are almost identical, demonstrating that the additional Fe contents observed to partition into $Al_2O_3$-bearing perovskite are approximately equal to the $Fe^{3+}$ concentrations. Therefore, within the precision of our experiments, the addition of $Al_2O_3$ to perovskite seems to only influence the $Fe^{3+}$ partitioning between perovskite and magnesiowüstite and does not affect the $Fe^{2+}$ concentration in each phase.

In Fig. 8b the Si content of perovskite is plotted against the combined $Fe^{3+}$ and Al concentrations. The two solid lines show the trends expected for substitution of $A^{3+}$ atoms (where $A^{3+} = Fe^{3+} + Al^{3+}$) via the $A_2O_3$ component, i.e. 3+ atoms in both eight-fold (normally occupied by $Mg^{2+}$) and six-fold (normally $Si^{4+}$) coordinated perovskite sites, and also for the $MgAO_{2.5}$ component, i.e. a 3+ atom only on the six-fold site. For lower $A^{3+}$ cation concentrations the data fall between both substitution mechanisms, although uncertainties here are high due to the relatively low concentrations, however, as $A^{3+}$ cation concentrations increase the data fall much closer to the $A_2O_3$ component mechanism. Previous studies [26,27] have indicated that Al may substitute onto both sites (i.e. an $A_2O_3$ component), while for $Al_2O_3$-free perovskite $Fe^{3+}$ apparently substitutes onto the six-fold coordinated site balanced by an oxygen vacancy [28]. The non-linear $Fe^{3+}$ versus Al trend in Fig. 8a implies, however, that the substitution mechanism is changing with $A^{3+}$ cation concentration, this is also inferred by Fig. 8b. This could result from $Fe^{3+}$ substitution onto the six-fold site for low $Al_2O_3$ concentrations, as observed for $Al_2O_3$-free perovskite [28], but onto both sites at higher $Al_2O_3$ contents. A further possibility that leads on from this is that at high $Al_2O_3$ contents substitution of a $FeAlO_3$ component occurs, where $Fe^{3+}$ preferentially substitutes onto the eight-fold site and is charge balanced by Al on the six-fold site. This is consistent with the observations in Fig. 8a where $Fe^{3+}$ is initially weakly correlated with Al, which would be expected if it were only entering the six-fold site, but a much stronger correlation occurs for higher Al contents, as $FeAlO_3$ substitution becomes the dominant mechanism. $FeAlO_3$ substitution makes crystallographic sense because the cation–site size mismatch is almost the same for $Fe^{3+}$ on the eight-fold site as it is for Al on the six-fold site [29], which is not the case for the opposite $AlFeO_3$ scenario where Al is on the eight-fold site. Atomistic computer simulations have also shown the $FeAlO_3$-coupled substitution mechanism to be the most energetically favourable for the incorporation of Al and $Fe^{3+}$ into perovskite [30].

The 660 km seismic discontinuity is widely believed to result from the breakdown of ringwoodite to produce magnesiowüstite and perovskite via the reaction:

$$(Mg,Fe)_2SiO_{4\,ringwoodite} = (Mg,Fe)SiO_{3\,perovskite} + \underset{magnesiowüstite}{(Mg,Fe)O} \quad (6)$$

This discontinuity is apparently sharp, i.e. it occurs over a narrow pressure interval, and this is consistent with partitioning experiments in the $Al_2O_3$-free system that show the Fe/(Fe+Mg) ratio of ringwoodite to be close to the combined Fe/(Fe+Mg) ratio of coexisting magnesiowüstite and perovskite. A sharp almost univariant transformation occurs because Fe is partitioned almost equally between both sides of Eq. 6. With the addition of $Al_2O_3$ to the system, however, Fe partitions more favourably into perovskite, which increases the Fe partitioning onto the right hand side of Eq. 6 and the pressure interval of the reaction would be broadened. As perovskite would contain $Al_2O_3$ at the '660', this may be inconsistent with a sharp discontinuity. Wood [12] proposed, however, that because the solubility of $Al_2O_3$ in perovskite is relatively low at pressures corresponding to the '660', the phase relations at

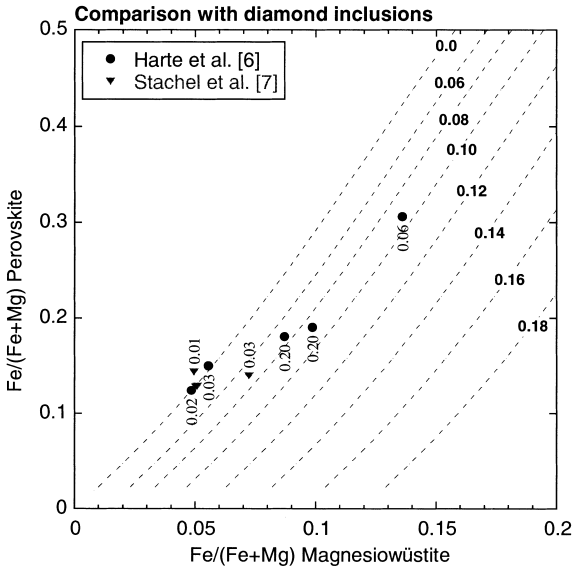


Fig. 9. A comparison of Fe–Mg partitioning between coexisting (Mg,Fe)O, (Mg,Fe)$SiO_3$ and (Mg,Fe,Al)(Al,Si)$O_3$ inclusions in diamonds proposed to come from the lower mantle, with the parameterisation from our study. The Al contents of the proposed perovskite inclusions are shown above/below each data point in atoms per formula unit.

these conditions would not be significantly different to those in the $Al_2O_3$-free system, thus preserving a sharp discontinuity. These observations are supported and strengthened by our findings. Due to the non-linear dependence of $Fe^{3+}$ on Al, the effect on the Fe–Mg partitioning would be relatively small for the perovskite $Al_2O_3$ contents expected at the '660' ($<2$ wt%). Further, as $Al_2O_3$ only seems to influence the $Fe^{3+}$ partitioning, and not $Fe^{2+}$, then any effect on the '660' is also likely to be small because the average mantle probably has a relatively low $Fe^{3+}/\Sigma Fe$ ratio [3].

## 6. Implications for deep mantle diamond inclusions

Analyses of mantle xenoliths suggest that the upper mantle has quite a low $Fe^{3+}/\Sigma Fe$ ratio, perhaps as low as 2% [3]. If the lower mantle possesses a similar $Fe^{3+}/\Sigma Fe$ ratio then lower mantle perovskite should be relatively poor in $Fe^{3+}$. One might, therefore, conclude that our partitioning results, being probably at conditions of $Fe^{3+}$ saturation in the perovskite structure, have little application to the Earth's mantle. The only samples currently available that may originate from the lower mantle are inclusions found in diamonds. Several diamonds have been identified which contain assemblages of (Mg,Fe,Al)(Al,Si)$O_3$ pyroxene and $Al_2O_3$-free pyroxene that it has been argued originally crystallised as silicate perovskite in the lower mantle [5–7]. Magnesiowüstite inclusions are also present in many of these diamonds. Mössbauer spectroscopy on some pyroxene inclusions has revealed remarkably high $Fe^{3+}/\Sigma Fe$ ratios of over 70% in one aluminous sample and a trend between the $Fe^{3+}/\Sigma Fe$ ratio and the $Al_2O_3$ content has also been observed [31]. The $Fe^{3+}/\Sigma Fe$ ratios of several inclusions are, therefore, similar to those measured in our experiments. In Fig. 9 we compare compositions of (Fe,Mg)O and (Mg,Fe,Al)(Al,Si)$O_3$ inclusions found in the same diamonds from Sao Luiz and Kankan with our parameterised results, in order to test if the Fe–Mg partitioning between these inclusions is consistent with an origin in the lower mantle. It should be stressed that no inclusions have been found that possess the structure of silicate perovskite and they are reported as being pyroxenes, however, perovskite would be expected to back transform to a lower pressure structure as it is very unstable outside of its stability field. Many of the inclusions with low $Al_2O_3$ contents are in excellent agreement with our experimental data but inclusions with intermediate and high $Al_2O_3$ contents show quite poor agreement with our results. The Fe/(Fe+Mg) ratios for (Mg,Fe,Al)(Al,Si)$O_3$ inclusions containing 0.2 formula units of Al should be significantly higher than observed according to our results. In Fig. 9 we have also plotted the $Fe^{3+}$ and Al contents in formula units for inclusions BZ251B and BZ210B [6]. Both inclusions plot below the substitution trend displayed by the experimental data. Although the $Fe^{3+}/\Sigma Fe$ ratio of inclusion BZ210B is relatively high (70%), the Fe/(Fe+Mg) ratio is lower than expected for a perovskite containing this much $Al_2O_3$, if it formed at similar conditions encountered in our experiments. We cannot of course exclude the possibility that the inclusions equilibrated in the lower mantle at conditions that were

not covered in our study. At higher pressure, for example, the apparent coupled substitution of Al and $Fe^{3+}$ inferred by our study may not occur. Computer simulations, however, suggest that this does remain the most favourable mechanism for Al and $Fe^{3+}$ substitution into perovskite to pressures of at least 100 GPa [30].

## 7. Summary

Fe–Mg partitioning experiments were performed between perovskite and magnesiowüstite in the 24–25 GPa pressure range in $Al_2O_3$-bearing and $Al_2O_3$-free systems. Re capsules were used to provide a relatively oxidising environment for the experiments.

Reversal and time study experiments indicate that run times of at least 8 h at 1650°C are required for Fe–Mg equilibrium to be achieved under relatively oxidising conditions. Preliminary experiments performed at lower $fo_2$ in the presence of metallic Fe, however, reveal equilibration times that are at least an order of magnitude slower than this. Reducing the $fo_2$ most likely lowers point defect concentrations in perovskite, resulting in very slow cation diffusion.

For $Al_2O_3$-free compositions Fe is preferentially partitioned into magnesiowüstite, in the ratio of approximately 3:1. As the maximum $Al_2O_3$ content of perovskite increases with pressure, we observe Fe to partition more equally between perovskite and magnesiowüstite.

The increase in the Fe/(Fe+Mg) ratio of perovskite for a given magnesiowüstite composition is a non-linear function of the perovskite $Al_2O_3$ concentration.

ELNES spectroscopy measurements of $Fe^{3+}/\Sigma Fe$ ratios show that the additional Fe that partitions into perovskite with increasing $Al_2O_3$ content is $Fe^{3+}$ and no effect on the $Fe^{2+}$ partitioning can be detected. $Fe^{3+}/\Sigma Fe$ ratios of $>80\%$ were observed for some $Al_2O_3$-rich perovskites. The dependence of the perovskite $Fe^{3+}$ solubility on the $Al_2O_3$ content is non-linear such that low $Al_2O_3$ concentrations have only a small effect on the $Fe^{3+}$ content.

The non-linear perovskite $Fe^{3+}$–Al dependence may result from $Fe^{3+}$ substitution switching from the six-fold site for low $Al_2O_3$ concentrations to a coupled $FeAlO_3$ component substitution at higher $Al_2O_3$ contents, where $Fe^{3+}$ is entirely on the eight-fold site charge balanced by $Al^{3+}$ on the six-fold site.

The Fe partitioning between some $(Mg,Fe)SiO_3$ and (Mg,Fe)O diamond inclusions is quite consistent with an origin in the lower mantle. However, the $(Mg,Fe,Al)(Al,Si)O_3$ inclusions examined do not show the same partitioning relations as observed in our experiments and do not follow the same Al–$Fe^{3+}$ substitution mechanism.

## Acknowledgements

We are grateful for discussions with C. McCammon, and T. Stachel. S. Mackwell is thanked for kindly providing magnesiowüstite starting powders. G. Herrmannsdörfer, H. Fischer, H. Schulze and D. Krausse are thanked for their invaluable technical assistance. The original manuscript benefited from the constructive reviews of J. Brodholt and an anonymous reviewer. *[BW]*

## References

[1] H.J. Reichmann, S.D. Jacobsen, S.J. Mackwell, C.A. McCammon, Sound wave velocities and elastic constants for magnesiowustite using gigahertz interferometry, Geophys. Res. Lett. 27 (2000) 799–802.

[2] Y.S. Xu, C. McCammon, B.T. Poe, The effect of alumina on the electrical conductivity of silicate perovskite, Science 282 (1998) 922–924.

[3] H.S.C. O'Neill, D.C. Rubie, D. Canil, C.A. Geiger, C.R. Ross, F. Seifert, A.B. Woodland, Ferric iron in the upper mantle and in transition zone assemblages: implications for relative oxygen fugacities in the mantle, Geophys. Monogr. 74 IUGG 14 (1993) 73–89.

[4] E. Ito, E. Takahashi, Postspinel transformations in the system $Mg_2SiO_4$–$Fe_2SiO_4$ and some geophysical implications, J. Geophys. Res. 94 (1989) 10637–10646.

[5] B. Harte, J.W. Harris, Lower mantle mineral associations preserved in diamonds, Mineral. Mag. 58A (1994) 384–385.

[6] B. Harte, J.W. Harris, M.T. Hutchison, G.R. Watt, M.C. Wilding, Lower mantle mineral associations in diamonds from São Luiz, Brazil, in: Y. Fei, C. Bertka, B.O. Mysen (Eds.), Mantle Mineralogy: Field Observations and High

Pressure Experimentation: A Tribute to Francis R. (Joe) Boyd, The Geochemical Society, Geochem. Soc. Spec. Publ. No. 6, Houston, TX, 1999, pp. 125–153.
[7] T. Stachel, J.W. Harris, G.P. Brey, W. Joswig, Kankan diamonds (Guinea) II: lower mantle inclusion parageneses, Contrib. Mineral. Petrol. 140 (2000) 16–27.
[8] Y. Fei, Solid solutions and element partitioning at high pressures and temperatures, in: R.J Hemley (Eds.) Ultrahigh-Pressure Mineralogy: Physics and Chemistry of the Earth's Deep Interior, Rev. Mineral 37, Mineral. Soc. Am., Washington, DC, 1999, 343–367.
[9] D. Andrault, Evaluation of (Mg,Fe) partitioning between silicate perovskite and magnesiowustite up to 120 GPa and 2300K, J. Geophys. Res. 106 (2001) 2079–2087.
[10] H.K. Mao, G. Shen, R.J. Hemley, Multivariable dependence of Fe-Mg partitioning in the lower mantle, Science 278 (1997) 2098–2100.
[11] B.J. Wood, D.C. Rubie, The effect of alumina on phase transformations at the 660-kilometer discontinuity from Fe-Mg partitioning experiments, Science 273 (1996) 1522–1524.
[12] B.J. Wood, Phase transformations and partitioning relations in peridotite under lower mantle conditions, Earth Planet. Sci. Lett. 174 (2000) 341–354.
[13] C. McCammon, Perovskite as a possible sink for ferric iron in the lower mantle, Nature 387 (1997) 694–696.
[14] S. Lauterbach, C.A. McCammon, P. van Aken, F. Langenhorst, F. Seifert, Mössbauer and ELNES spectroscopy of (Mg,Fe)(Si,Al)$O_3$ perovskite: a highly oxidised component of the lower mantle, Contrib. Mineral. Petrol. 138 (2000) 17–26.
[15] E. van Cappellen, J.C. Doukhan, Quantitative X-ray microanalysis of ionic compounds, Ultramicroscopy 53 (1994) 343–349.
[16] P.A. van Aken, B. Liebscher, V.S. Styrsa, Quantitative determination of iron oxidation states in minerals using Fe L2, 3-edge electron energy-loss near-edge structure spectroscopy, Phys. Chem. Min. 5 (1998) 323–327.
[17] R.F. Egerton, Electron Energy Loss Spectroscopy in the Electron Microscope, 2nd edn. Plenum, New York, 1996, 485 pp.
[18] B.J. Wood, Erratum to: 'Phase transformations and pationing relations in peridotite under lower mantle conditions' [Earth Planet. Sci. Lett. 174 (2000) 341–354], Earth Planet. Sci. Lett. 176 (2000) 543.
[19] T. Irifune, T. Koizumi, J.-i. Ando, An experimental study of the garnet-perovskite transformation in the system $MgSiO_3$–$Mg_3Al_2Si_3O_{12}$, Phys. Earth Planet. Int. 96 (1996) 147–157.
[20] K. Matsuzaka, M. Akaogi, T. Suzuki, T. Suda, Mg-Fe partitioning between silicate spinel and magnesiowüstite at high pressures: experimental determination and calculation of phase relations in the system $Mg_2SiO_4$–$Fe_2SiO_4$, Phys. Chem. Min. 27 (2000) 310–319.
[21] C.A. McCammon, J. Peyronneau, J.P. Poirier, Low ferric iron content of (Mg,Fe)O at high pressures and temperatures, Geophys. Res. Lett. 25 (1998) 1589–1592.
[22] D.J. Frost, F. Langenhorst, P.A. van Aken, Fe-Mg partitioning between ringwoodite and magnesiowüstite and the effect of pressure, temperature and oxygen fugacity, Phys. Chem. Min. 28 (2001) 455–470.
[23] C.K. Gessmann, D.C. Rubie, C.A. McCammon, Oxygen fugacity dependence of Ni, Co, Mn, Cr, V, and Si partitioning between liquid metal and magnesiowüstite at 9–18 GPa and 2200°C, Geochim. Cosmochim. Acta 63 (1999) 1853–1863.
[24] T. Katsura, E. Ito, Determination of Fe-Mg partitioning between perovskite and magnesiowüstite, Geophys. Res. Lett. 23 (1996) 2005–2008.
[25] T. Irifune, Absence of an aluminous phase in the upper part of the lower mantle, Nature 370 (1994) 131–133.
[26] J.F. Stebbins, S. Kroeker, D. Andrault, The mechanism of solution of aluminium oxide in $MgSiO_3$ perovskites, Geophys. Res. Lett. 28 (2001) 615–618.
[27] D. Andrault, D.R. Neuville, A.-M. Flank, Y. Wang, Cation sites in Al-rich $MgSiO_3$ perovskites, Am. Mineral. 83 (1998) 1045–1053.
[28] C.A. McCammon, The crystal chemistry of ferric iron in $Fe_{0.05}Mg_{0.95}SiO_3$ perovskite as determined by Mössbauer spectroscopy in the temperature range 80–293 K, Phys. Chem. Min. 25 (1998) 292–300.
[29] S.E. Kesson, J.D. Fitzgerald, J.M.G. Shelley, R.L. Withers, Phase relations, structure and crystal chemistry of some aluminous silicate perovskites, Earth Planet. Sci. Lett. 134 (1995) 187–201.
[30] N.C. Richmond, J.P. Brodholt, Calculated role of alumina in the incorporation of ferric iron into magnesium silicate perovskite, Am. Mineral. 83 (1998) 947–951.
[31] C. McCammon, M. Hutchison, J. Harris, Ferric iron content of mineral inclusions in diamonds from São Luiz: A view into the lower mantle, Science 278 (1997) 434–436.